

# Fluorine-Induced Molybdate Trap-and-Buffer Enables Durable Intermittent Alkaline Seawater Electrolysis

Dengyu Fu, Xiaogang Sun, Fei-Yue Gao, Yao Zheng,\* and Shi-Zhang Qiao\*

**Electrodes' stability under intermittent operation remains a key bottleneck for alkaline seawater electrolysis. Especially, the cathode typically undergoes self-oxidation under constant-current operation, while this process intensifies during abrupt shutdown due to the presence of reverse current. Such accelerated cathodic degradation significantly undermines the long-term durability of the electrolyzer during practical operating. Here a fluorine-doped nickel-molybdenum oxide cathode is reported that maintains stability under both constant-current operation and startup-shutdown transitions. This full-cycle stability is achieved through a vacancy-mediated molybdate trap-and-buffer strategy. Vacancies generated by fluorine leaching under constant-current operation strongly trap molybdates, forming a negatively charged interfacial layer. This electron-enriched layer effectively buffers the active sites against overoxidation during abrupt shutdown. Meanwhile, its strong electrostatic-repulsion capability suppresses further dissolving of molybdenum and protects the electrode from chloride ion attack. As a result, an alkaline seawater electrolyzer assembled with the target catalyst operates stably for over 500 h at constant-current densities of 0.5 and 1.0 A cm<sup>-2</sup>. Notably, the electrolyzer maintains stable performance over 3900 startup-shutdown cycles with a minimal voltage degradation of only 0.02 mV per cycle.**

## 1. Introduction

Alkaline seawater electrolysis has emerged as a promising and cost-effective route for large-scale hydrogen production.<sup>[1-3]</sup> Practical seawater electrolysis powered by renewable energy is not limited to constant-current operation but also involves frequent startup-shutdown transitions due to the intermittent nature of renewable power sources. Therefore, ensuring the full-cycle operational stability of electrodes is of critical importance. Currently, most studies focus on anodic challenges in seawater electrolysis with considerable advances.<sup>[4,5]</sup> However, systematic investigations into cathodic stability under practical conditions remain scarce. Given that cathodes suffer even more pronounced

corrosion under the intermittent operating conditions, this highlights the urgent need for durable cathodic catalysts.

Among various alkaline hydrogen evolution catalysts, NiMo-based materials have stood out due to their high intrinsic activity, favorable conductivity, and industrial feasibility.<sup>[6-8]</sup> However, the Mo component is thermodynamically unstable in alkaline media, where it tends to leach out as soluble molybdate ion ( $\text{MoO}_4^{2-}$ ) during prolonged operation.<sup>[7,9,10]</sup> This continuous loss of Mo not only depletes active sites, but also leads to structural collapse and interfacial instability, ultimately impairing hydrogen evolution reaction (HER) performance. Such degradation has already been observed under constant-current operation, potentially posing even greater risks under intermittent conditions. To mitigate Mo leaching under steady-state conditions, various strategies such as surface coating,<sup>[11]</sup> heterostructure design,<sup>[12]</sup> and anion regulation have been explored.<sup>[13]</sup> Although these strategies, primarily based on surface passivation or interfacial charge modulation, show initial effectiveness, most fail to

sustain Mo retention beyond a few hundred hours under alkaline conditions.<sup>[14,15]</sup>

More critically, practical intermittent operating conditions further accelerate catalyst deactivation and structural decay.<sup>[16]</sup> Specifically, during shutdown periods, the removal of external bias allows a potential imbalance between electrodes, resulting in reverse current flow from anode to cathode.<sup>[17,18]</sup> This leads to a positive (i.e., less negative) shift of the cathode potential, which promotes the self-oxidation of active metal sites and ultimately causes structural degradation.<sup>[19]</sup> Simultaneously, chloride ions ( $\text{Cl}^-$ ) in seawater readily adsorb onto and attack the cathode surface, leading to further corrosion of the catalyst.<sup>[20,21]</sup> These coupled degradation pathways will further undermine the long-term stability of the catalyst. However, to date, no studies have specifically addressed the stability challenges of NiMo-based catalysts under startup-shutdown conditions, which limits the development of durable catalyst systems designed for practical seawater electrolysis.

Here, we achieved the full-cycle operating stability of the NiMo cathode through fluorine-doping. An initial fluorine leaching process under constant-current conditions induces the formation of surface oxygen vacancies, which act as charge-imbalanced sites

D. Fu, X. Sun, F.-Y. Gao, Y. Zheng, S.-Z. Qiao

School of Chemical Engineering  
The University of Adelaide  
Adelaide, SA 5005, Australia

E-mail: [yao.zheng01@adelaide.edu.au](mailto:yao.zheng01@adelaide.edu.au); [s.qiao@adelaide.edu.au](mailto:s.qiao@adelaide.edu.au)

 The ORCID identification number(s) for the author(s) of this article can be found under <https://doi.org/10.1002/adfm.202526332>

DOI: 10.1002/adfm.202526332

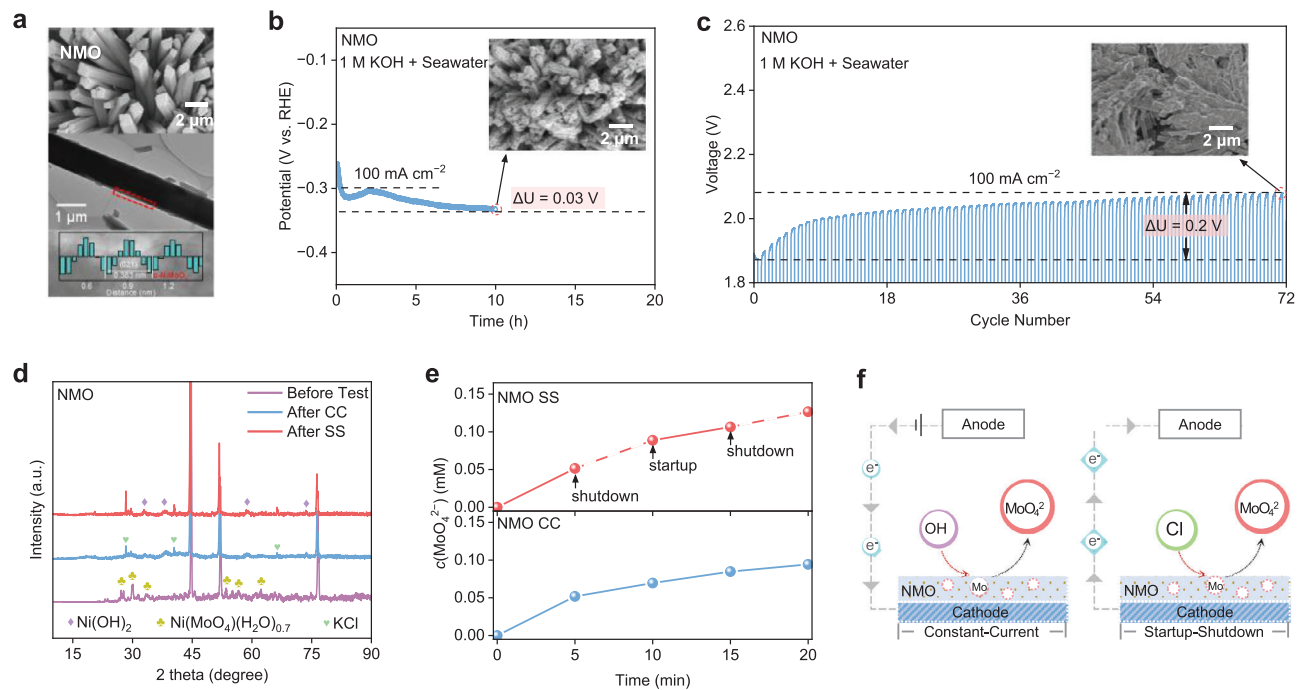


**Figure 1.** a) SEM and Transmission electron microscope (TEM) image of NMO. b) Accelerated stability test of NMO in 1 M KOH + seawater at 80 °C under 100 mA cm<sup>-2</sup> constant-current conditions, no *iR*-compensation for potential, an inset SEM image showed NMO morphology after constant-current tests. c) Stability test of NMO cathode paired with an Ir-Ta plate anode in 1 M KOH + seawater at 80 °C under 100 mA cm<sup>-2</sup>, with cyclic startup-shutdown operation every 10 min, no *iR*-compensation for voltages, an inset SEM morphology image showed NMO after startup-shutdown tests. d) XRD patterns of NMO before and after constant-current (CC) and startup-shutdown (SS) reaction in alkaline seawater. e) MoO<sub>4</sub><sup>2-</sup> dissolution under constant-current and startup-shutdown conditions. f) Schematic illustration of OH<sup>-</sup>/Cl<sup>-</sup>-induced degradation of NMO during alkaline seawater HER and shutdown phase.

to anchor molybdate species. On the one hand, these anchored anions effectively suppress the continues leaching of Mo during constant-current operation and preserve the structural integrity of the catalyst; on the other hand, under intermittent startup-shutdown conditions, the interfacial molybdate layer further acts as an electron reservoir and a chloride-repelling barrier, mitigating cathodic oxidation and Cl<sup>-</sup>-induced corrosion. Benefiting from this molybdate trap-and-buffer mechanism, the target cathode delivers 500 h of constant-current stability at 0.5/1 A cm<sup>-2</sup> in an alkaline electrolyzer and maintains its performance over 3900 startup-shutdown cycles.

## 2. Results and Discussion

### 2.1. Degradation of NiMo-Based Catalyst During HER

To uncover the degradation behavior of NiMo-based catalysts under practical alkaline seawater HER conditions, nickel-molybdenum oxide (NMO) was selected as a representative material and synthesized via hydrothermal method followed by a calcination process. The pristine NMO exhibited a cubic-prismatic micro-scale rod-like structure (Figure 1a). The structural stability of this material under practical alkaline seawater condition was systematically studied under constant-current and startup-shutdown cycling conditions (Figures 1b,c, S1, Supporting Information). At a constant-current density of 100 mA cm<sup>-2</sup>, the overpotential of NMO rapidly increased over time, indicating fast de-

activation. The inset scanning electron microscopy (SEM) image further revealed significant surface etching, indicating substantial structural corrosion and degradation due to the dissolution of Mo species in the presence of OH<sup>-</sup>. Under accelerated startup-shutdown cycling tests, the NiMo-based two-electrode setup exhibited a significant voltage increase of ≈0.2 V within 72 cycles (Figure 1c), indicating a much faster degradation rate than that observed under constant-current operation. Correspondingly, the damage was more severe in the NMO, with the original cubic-prismatic rod-like structure completely collapsing (Figure 1c inset). These results indicate that higher current densities and intermittent startup-shutdown operation intensify the instability and dissolution of NMO surfaces.

X-ray diffraction (XRD) analysis identified the disappearance of the initial dominant Ni(MoO<sub>4</sub>)<sub>0.7</sub> phase in NMO after constant-current and startup-shutdown tests (Figure 1d),<sup>[22]</sup> confirming the significant structural degradation and phase transformation of the catalyst during HER. Ultraviolet-visible (UV-vis) spectrophotometry was employed to monitor the concentration of MoO<sub>4</sub><sup>2-</sup> in the electrolyte during alkaline HER (Figure 1e).<sup>[23,24]</sup> A gradual increase in MoO<sub>4</sub><sup>2-</sup> concentration was observed under constant-current conditions, consistent with near-surface OH<sup>-</sup>-driven conversion of Mo-O species into soluble molybdate; by contrast, startup-shutdown operation led to a more rapid accumulation, which can be attributed to the reverse current-driven Mo oxidation and Cl<sup>-</sup> attack. Additionally, ICP-MS analysis of acid-digested electrodes corroborates these trends,

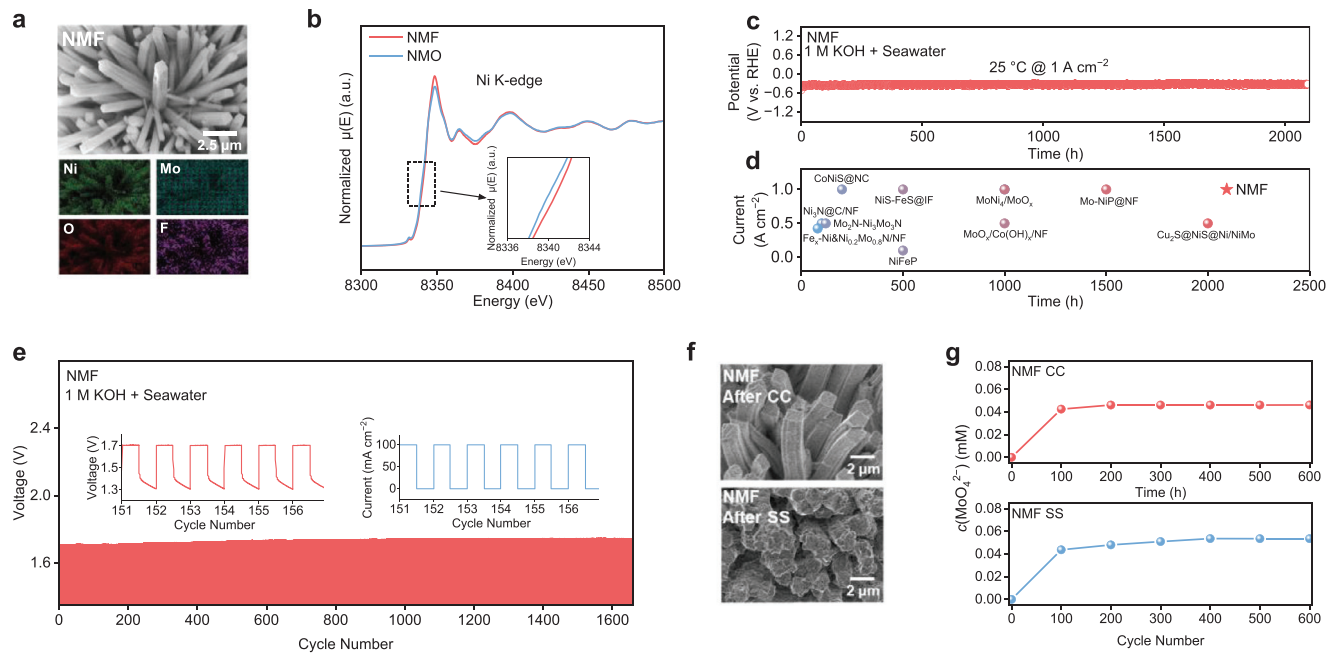


**Figure 2.** a) SEM image of the NMF and elemental mapping of Ni, Mo, and F. b) Ni K-edge hard XAS of NMO and NMF. c) Long-term stability test of NMF in 1 M KOH + seawater at room-temperature with 85%  $iR$  compensation for potential. d) Comparison of HER stability of different catalysts in alkaline seawater at various current densities. e) Stability test of NMF cathode paired with an Ir-Ta plate anode in 1 M KOH + seawater at 80 °C under 100  $\text{mA cm}^{-2}$  with cyclic startup-shutdown operation every 10 min, no  $iR$  compensation for voltage. f) SEM images of NMF after constant-current (CC) and startup-shutdown (SS) tests. g)  $\text{MoO}_4^{2-}$  concentration in electrolyte during constant-current and startup-shutdown stability tests for NMF.

revealing substantial Mo loss from NMO after both constant-current and, more severely, after startup-shutdown operation, whereas the Ni content remains essentially unchanged (Figures S2a,b, Supporting Information). These dissolution behaviors are summarized in the degradation scheme in Figure 1f, where  $\text{OH}^-$  under constant-current operation and the combined reverse-current/ $\text{Cl}^-$  effects under shutdown jointly drive Mo leaching.

## 2.2. Stability Enhancement of Fluorine-Doped NMO

To address the stability issue of NiMo-based catalysts caused by the rapid dissolution of Mo in practical operation, fluorine (F) doping was employed to obtain a modified nickel-molybdenum catalyst (Figure S3, Supporting Information). SEM images showed that the F-doped nickel-molybdenum oxide (NMF) maintained a micron-scale cuboid structure similar to NMO (Figure 2a). The F elemental mapping, together with the new peak at  $\approx 1.1 \text{ \AA}$  in the Ni K-edge extended X-ray absorption fine structure (EXAFS) R-space (Figure S4, Supporting Information), confirming the incorporation of fluorine.<sup>[25,26]</sup> Beyond structural incorporation, fluorine doping also modulated the electronic configuration of the metal centers. Ni 2p X-ray photoelectron spectroscopy (XPS) spectra and Ni L-edge soft X-ray absorption spectroscopy (XAS) spectra showed an increased  $\text{Ni}^{3+}/\text{Ni}^{2+}$  ratio (Figures S5 and S6, Supporting Information),<sup>[27,28]</sup> while Mo 3d XPS revealed a weakened  $\text{Mo}^{5+}$  signal (Figure S7, Supporting Information).<sup>[29,30]</sup> In addition, the enhanced white line intensity in the Ni and Mo K-edge X-ray absorption near-edge structure (XANES) spectra (Figures 2b; S8, Supporting Information)

further supports the presence of F-induced electron deficiency at the metal centers.<sup>[31,32]</sup> Moreover, split Mo-O shells in R-space EXAFS ( $\approx 0.8/1.4 \text{ \AA}$ ), intensified defect features in O K-edge XAS/O 1s XPS, and broadened Raman bands (Figures S9–S12, Supporting Information) collectively indicate markedly increased structural disorder.<sup>[33–38]</sup> These results suggest that F doping withdraws electrons from adjacent metal centers, leading to the formation of locally electron-rich F sites and electron-deficient metal regions. This redistribution of charge weakens metal–oxygen bonds and can facilitate the formation of oxygen vacancies under electrocatalytic conditions.

The effect of fluorine doping on HER performance was then investigated in alkaline seawater. NMF demonstrated superior alkaline HER activity and stability relative to NMO (Figure S13, Supporting Information), achieving a current density of  $1 \text{ A cm}^{-2}$  at an overpotential of only 323 mV, lower than that of NMO (368 mV). Besides, NMF delivers faster HER kinetics and higher active-surface utilization than NMO, as evidenced by a lower Tafel slope ( $81 \text{ s } 195 \text{ mV dec}^{-1}$ ), a much smaller EIS semicircle, larger  $C_{dl}$ -derived ECSA ( $3.78 \text{ vs } 2.22 \text{ mF cm}^{-2}$ ), and higher  $\text{H}_2$  Faradaic efficiency approaching 100% at  $0.5\text{--}1 \text{ A cm}^{-2}$  (Figures S14–S17, Supporting Information). Notably, NMF operated stably for over 2,000 h at a high current density of  $1 \text{ A cm}^{-2}$  (Figure 2c). This remarkable durability surpasses that of several reported cathodes utilized in alkaline seawater electrolysis (Figure 2d).<sup>[39–48]</sup> Furthermore, NMF maintained outstanding stability under more extreme startup-shutdown conditions, exhibiting only a slight increase in startup voltage over 1600 startup-shutdown cycles (Figure 2e). Multi-step chronopotentiometry (CP) was carried out by stepping the current density between discrete values within

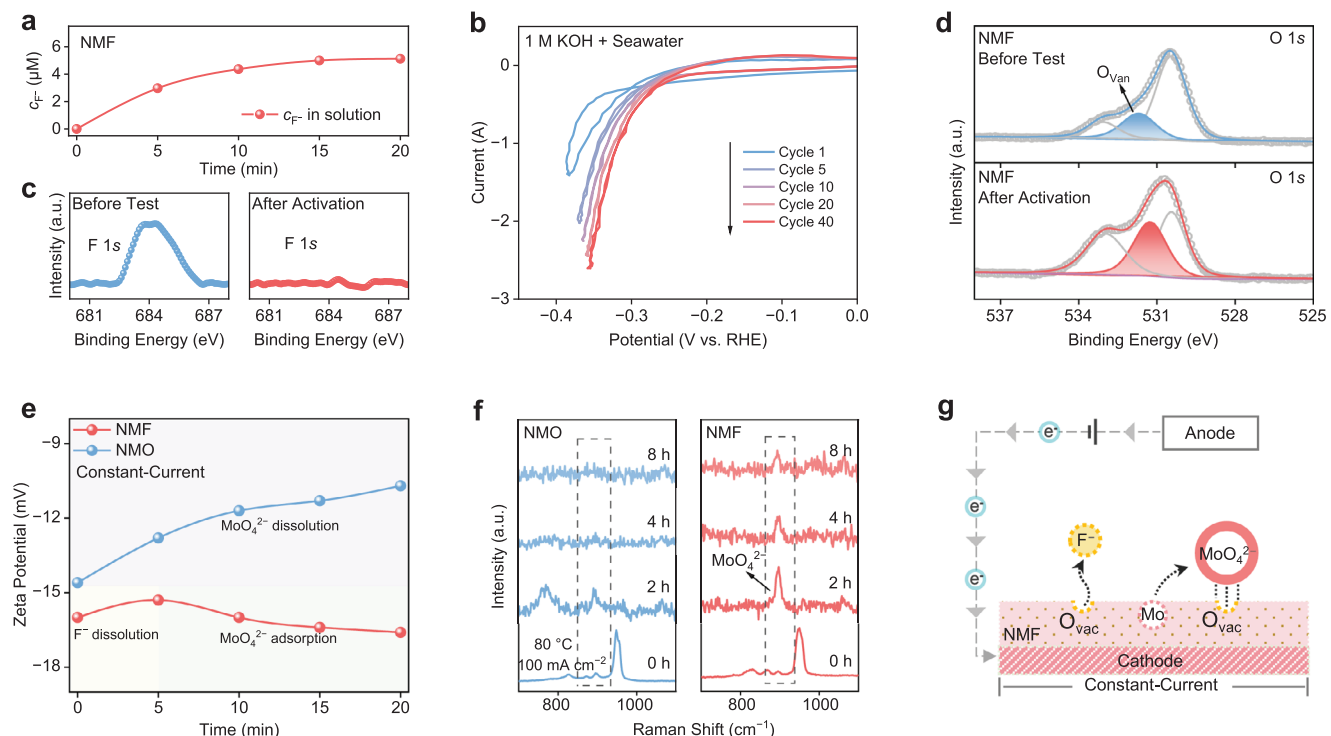


**Figure 3.** a) F<sup>-</sup> concentration in the electrolyte during the reaction process of NMF. b) Cyclic voltammetry curves of NMF during the activation process, with current integration correction. c) XPS spectra of F 1s for NMF before and after activation (i.e., after a period of electrochemical reaction). d) XPS spectra of O 1s for NMF before and after activation. e) Zeta potential of NMO and NMF at different stages during constant-current testing (80 °C, 100 mA cm<sup>-2</sup>) in a model electrolyte of 1.0 M KOH + 0.5 M NaCl, chosen to emulate the chloride activity and ionic strength of the alkaline seawater catholyte at pH 14. f) In situ Raman spectra of NMO and NMF at different reaction stages under 80 °C, 1 M KOH + seawater, 100 mA cm<sup>-2</sup>. g) Schematic illustration of the surface transformation of NMF during constant-current HER operation.

the HER operating range and repeating the eight-step sequence for over 420 cycles (Figure S18, Supporting Information). Despite prolonged stability testing, NMF maintained its original morphology (Figure 2f). While slight surface roughening was observed after the startup-shutdown test, the overall structural integrity was well preserved. Meanwhile, UV-vis spectra showed that the MoO<sub>4</sub><sup>2-</sup> concentration in the electrolyte from NMF remained very low throughout both 600 h of constant-current operation and 600 startup-shutdown cycles (Figure 2g). This indicated that fluorine doping effectively suppresses Mo dissolution, thereby contributing to the long-term stability of NMF in full-cycle operation.

### 2.3. Origin of Stability Enhancement at Steady State

To elucidate the origin of suppressed Mo dissolution, we first monitored the concentration variation of fluoride ion (F<sup>-</sup>) during constant-current HER via ion chromatography. As shown in Figure 3a, a rapid increase in F<sup>-</sup> concentration was observed at the early stage of electrolysis, indicating progressively release of F from the crystal structure during HER. This early F loss was accompanied by a steady increase in current density observed in cyclic voltammetry (Figure 3b), suggesting gradual surface activation. XPS analysis further supported this process, with the F 1s signal nearly disappearing after activation (Figure 3c).<sup>[49,50]</sup> Si-

multaneously, O 1s spectra showed a significant increase in the vacancy-related component (Figure 3d),<sup>[35,36]</sup> confirming the formation of oxygen vacancies induced by fluorine leaching. Consistently, Electron Paramagnetic Resonance (EPR) spectroscopy of the electrochemically activated samples (Figure S19, Supporting Information) reveals a pronounced g ≈ 2.003 signal for F-doped NMF, typically associated with oxygen-vacancy-related centers in transition-metal oxides, whereas undoped NMO shows only a negligible response, indicating a substantially higher oxygen-vacancy density in NMF.<sup>[51,52]</sup> Given that fluorine atoms initially withdraw electrons from neighboring Ni and Mo centers (Figures S6–S10, Supporting Information), their subsequent removal generates locally electron-deficient defect sites, which create favorable conditions for stabilizing molybdate species through electrostatic interaction.

To further examine the proposed role of oxygen vacancies in anchoring MoO<sub>4</sub><sup>2-</sup> species, we investigated surface charge dynamics through zeta potential measurements.<sup>[53,54]</sup> For NMO, the zeta potential gradually shifted from -14 to -10 mV during the reaction (Figure 3e), which can be attributed to the continuous dissolution of MoO<sub>4</sub><sup>2-</sup>. The loss of these surface-bound anions reduced local negative charge, resulting in a less negative zeta potential. In contrast, the zeta potential of NMF, after a slight initial increase from -16 to -15 mV, showed a gradual decrease in dominated trend. This behavior suggests that the early release of F<sup>-</sup> temporarily reduced the surface negative charge

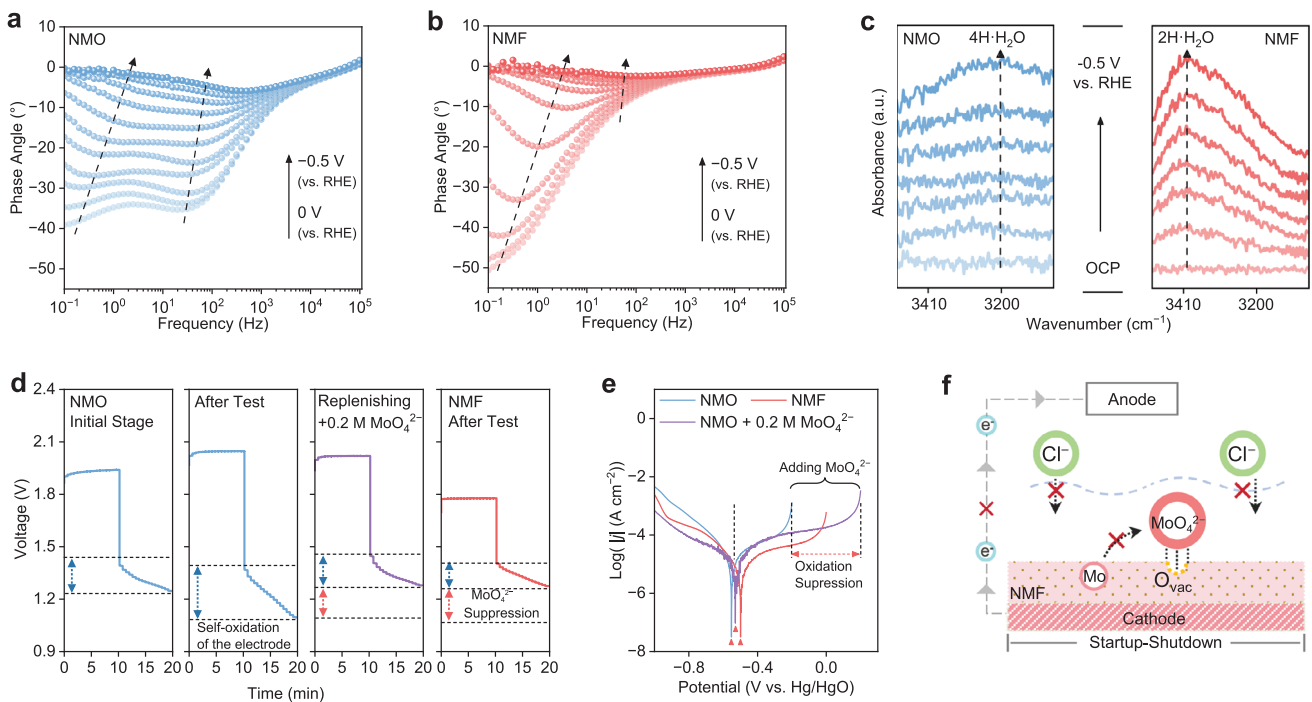


**Figure 4.** In situ phase angle variations of a) NMO and b) NMF at different potentials. c) In situ infrared (IR) spectra of NMO and NMF in alkaline seawater electrolyte. d) Open-circuit voltage variations of NMO and NMF at different stages during startup-shutdown cycling, no *iR* compensation for voltage. e) Comparison of Tafel plots for NMO, NMF, and NMO with additional MoO<sub>4</sub><sup>2-</sup> in 1 M KOH + seawater electrolyte, no *iR* compensation for potential. f) Schematic illustration of the shutdown state stability and protection mechanism of NMF.

density, while the subsequent formation of oxygen vacancies allowed MoO<sub>4</sub><sup>2-</sup> to be anchored on the surface, thereby leading to a more negative zeta potential over time. To gain further insight into the surface behavior of MoO<sub>4</sub><sup>2-</sup>, in situ Raman spectroscopy was performed at different stages of the reaction. The characteristic Raman peak at 900 cm<sup>-1</sup>, corresponding to MoO<sub>4</sub><sup>2-</sup> species,<sup>[10,55]</sup> appears transiently on NMO and then rapidly diminishes (Figure 3f), which we attribute to an on-surface dissolution intermediate that is subsequently lost to the electrolyte. By contrast, NMF displays a much stronger MoO<sub>4</sub><sup>2-</sup> band at early times, which remains detectable throughout the reaction window despite a moderate decrease in intensity. Combined with the zeta potential evolution and the only slight decrease in Mo content revealed by ICP-MS for NMF, this behavior suggests that in NMF the in situ generated MoO<sub>4</sub><sup>2-</sup> species are largely retained at F-induced oxygen-vacancy sites and undergo gradual restructuring rather than complete dissolution. These observations collectively suggest that fluorine doping promotes the formation of surface oxygen vacancies, which serve to trap in situ generated MoO<sub>4</sub><sup>2-</sup> species, thereby suppressing the continuous Mo leaching and maintaining operational stability (Figure 3g).

#### 2.4. Origin of Stability Enhancement During Abrupt Shutdown

To uncover the origin of NMF's startup-shutdown stability, we investigated interfacial charge behavior and surface ion dynamics following abrupt HER shutdown. In situ Bode phase plots were collected to evaluate the frequency-dependent interfacial polar-

ization characteristics of NMO and NMF (Figure 4a,b). In the mid-frequency range (10–1000 Hz), the NMO electrode exhibited large phase angles initially, which decreased sharply from  $-40^\circ$  to  $-5^\circ$  with increasing potential, indicating pronounced interfacial polarization and capacitive charge accumulation.<sup>[56,57]</sup> Such charge buildup induced voltage spikes and transient reverse currents upon abrupt HER shutdown, accelerating surface oxidation and Mo leaching. In contrast, the NMF electrode maintained near-zero phase angles across the same potential range, reflecting minimal interfacial polarization and more efficient charge dissipation. At low frequencies (0.1–1 Hz), the steeper phase angle decline observed for NMF reflected a faster transition to Faradaic charge transfer,<sup>[58]</sup> enabling more complete discharge of residual surface charges during the shutdown phase. This rapid charge release was essential for stabilizing interfacial potential and reducing reverse current under abrupt shutdown conditions.

To elucidate the interfacial structural features responsible for the enhanced interfacial charge dissipation behavior in NMF, in situ IR spectroscopy was performed (Figure 4c). A clear blueshift of the O-H stretching band from  $\approx 3200$  to  $\approx 3410$  cm<sup>-1</sup> was observed for NMF, indicating weakened hydrogen bonding and the formation of more loosely bound interfacial water.<sup>[59]</sup> This hydration layer reorganization was attributed to MoO<sub>4</sub><sup>2-</sup> species anchored at oxygen vacancy sites, which together constructed a negatively charged interfacial shell capable of buffering electrons and dissipating accumulated charges during shutdown. The structural retention of this interfacial shell was corroborated by Raman spectra, which showed persistent MoO<sub>4</sub><sup>2-</sup> signals after HER cycling (Figure S20, Supporting Information), and by zeta

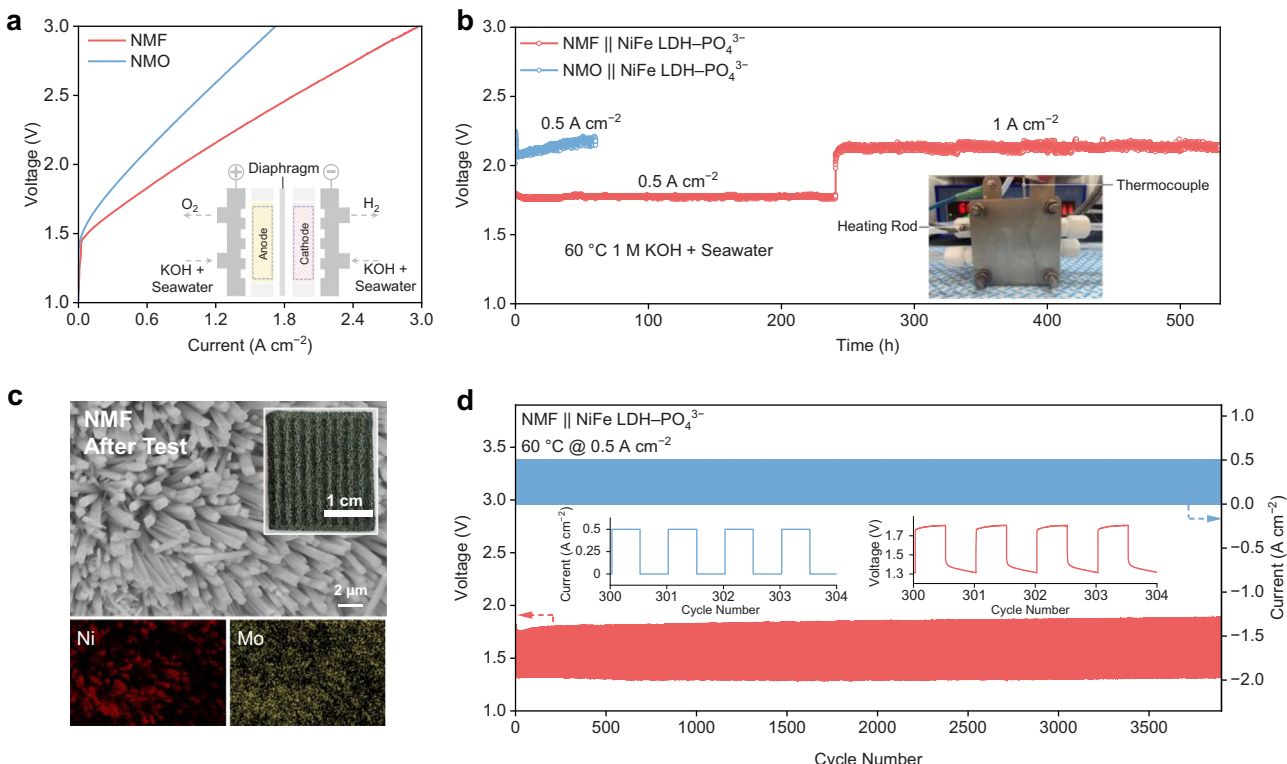


**Figure 5.** a) Polarization curves of ASWE assembled with NMO and NMF as the cathode and NiFe LDH–PO<sub>4</sub><sup>3-</sup> as the anode at 60 °C, schematic illustration of ASWE, no *iR* compensation for voltages. b) Durability test of ASWE assembled with NMO and NMF as the cathode and NiFe LDH–PO<sub>4</sub><sup>3-</sup> as the anode at 0.5/1.0 A cm<sup>-2</sup>, optical image of ASWE, no *iR* compensation for voltage. c) SEM images of the NMF cathode after the constant-current stability test, with the inset showing an optical image and elemental mapping of Ni and Mo. d) Stability test of NMF cathode coupled with NiFe LDH–PO<sub>4</sub><sup>3-</sup> anode in 1 M KOH + seawater at 60 °C under 0.5 A cm<sup>-2</sup> with cyclic startup-shutdown operation every 5 min, no *iR* compensation for voltage.

potential measurements, which revealed a consistently negative surface charge (Figure S21, Supporting Information). Ex situ Mo 3d and Ni 2p XPS of NMF across the pristine, after-startup, and after-shutdown states (Figure S22, Supporting Information) are consistent with this picture: the Mo 3d main peak undergoes a small positive binding-energy shift during startup that only partially relaxes after shutdown, whereas Ni 2p and the surface Mo/Ni ratio remain nearly unchanged. These reversible Mo 3d shifts indicate in-place electronic/coordination adjustment of surface molybdate species anchored at F-induced oxygen vacancies, in line with their role as an interfacial electron-buffering layer under shutdown conditions.

The impact of this effect on intermittent operating stability was reflected in the voltage response of the electrodes under accelerated startup-shutdown cycling mode (10 min on, 10 min off, Figure 4d). The NMO electrode showed steeper open-circuit voltage (OCV) drop over cycles, associated with progressive MoO<sub>4</sub><sup>2-</sup> leaching and destabilized surface charge regulation. In contrast, the NMF electrode exhibited significantly smoother OCV fluctuations during the shutdown phase. Notably, the addition of 0.2 M MoO<sub>4</sub><sup>2-</sup> to the NMO electrolyte also markedly suppressed OCV fluctuations. These results confirm that surface MoO<sub>4</sub><sup>2-</sup> species buffer interfacial charge accumulation, thereby suppressing reverse current generation and improving shutdown-state stability. The resulting oxidative resistance of the electrodes was evaluated by Tafel polarization analysis (Figure 4e). The NMF elec-

trode exhibited a more gradual anodic slope and a more positive corrosion potential (−0.50 V vs Hg/HgO) compared to NMO (−0.55 V vs Hg/HgO), indicating reduced oxidation tendency and enhanced corrosion resistance.<sup>[60]</sup> Similarly, incorporating 0.2 M MoO<sub>4</sub><sup>2-</sup> into the NMO electrolyte not only suppressed anodic current response but also shifted the corrosion potential positively, further confirming the protective role of surface MoO<sub>4</sub><sup>2-</sup> species in stabilizing the electrode interface.

Moreover, since the cathode is susceptible to chloride-induced corrosion under shutdown conditions, we further simulated this scenario by immersing the electrodes in 0.5 M NaCl at 60 °C for 48 h. As a result, the NMO electrode exhibited extensive surface collapse and severe morphological disintegration, as indicated by the complete loss of NiMoO<sub>x</sub> crystallinity (Figures S23 and S24, Supporting Information). In contrast, the NMF electrode retained its well-defined rod-like morphology and distinct NiMoO<sub>x</sub> diffraction peaks. In addition, the retention of MoO<sub>4</sub><sup>2-</sup> on NMF was confirmed by Raman spectra (Figure S25, Supporting Information), suggesting a protective mechanism enabled by stably anchored molybdate species. Collectively, the improved shutdown state stability of NMF can be attributed to the multifunctional behavior of surface-anchored MoO<sub>4</sub><sup>2-</sup>. The interfacial MoO<sub>4</sub><sup>2-</sup> forms an interfacial electron-buffering layer that not only facilitates rapid charge dissipation and mitigates charge-induced surface oxidation, but also repels chloride ions through electrostatic effects (Figure 4f).

## 2.5. Practical Application of NMF

We further evaluated the practical operation stability of NMF in an alkaline seawater electrolyzer (ASWE). The overall electrochemical performance of the NMO and NMF electrolyzers was initially compared at 60 °C (Figure 5a). NMF exhibited superior performance compared to NMO, achieving a cell voltage of 2.05 V at 1 A cm<sup>-2</sup>. Besides, the NMF-based electrolyzer exhibited markedly improved performance with increasing temperature (Figure S26, Supporting Information). The long-term stability of NMO and NMF was then evaluated at constant-current densities of 0.5 and 1 A cm<sup>-2</sup>. NMF demonstrated continuous operation for over 500 h with negligible degradation, while NMO exhibited poor stability at 0.5 A cm<sup>-2</sup> with rapid performance decay. After the stability test, the NMF cathode largely retained its initial micro-scale rod-like structure, with Ni and Mo remaining uniformly distributed (Figure 5c).

Raman spectrum confirmed that surface MoO<sub>4</sub><sup>2-</sup> was still detectable after stability testing (Figure S27, Supporting Information). Furthermore, to simulate the frequent startup-shutdown cycles in real industrial applications, a long-term accelerated startup-shutdown cycling test was conducted (Figure 5d). At 60 °C and a startup current density of 0.5 A cm<sup>-2</sup>, the electrolyzer maintained excellent stability for over 3900 startup-shutdown cycles (equivalent to ≈650 h), with a minimal voltage decay of only 0.02 mV per cycle. These results strongly demonstrate the full-cycle robustness of NMF under intermittent operating conditions, highlighting its practical viability for industrial applications.

## 3. Conclusion

We demonstrate that fluorine-doped nickel-molybdenum oxide can effectively address stability challenges in alkaline seawater HER. Fluorine incorporation induces oxygen vacancies that serve as robust anchoring sites for MoO<sub>4</sub><sup>2-</sup> species, which play dual roles in stabilizing the catalyst. Under constant-current conditions, the anchored molybdates suppress Mo dissolution and preserve the active surface composition. During intermittent startup-shutdown operation, they further act as an interfacial electron-buffering shell that mitigates self-oxidation of active metal centers and inhibits chloride-induced corrosion. The NMF cathode achieved exceptional durability in ASWE, maintaining stable performance over 3900 startup-shutdown cycles and prolonged high-current operation, with a minimal voltage decay of only 0.02 mV per cycle at 0.5 A cm<sup>-2</sup>. This work demonstrates an effective interfacial engineering strategy for stabilizing NiMo-based catalysts under intermittent seawater electrolysis, paving the way toward practical hydrogen production in renewable-energy-powered systems.

## Supporting Information

Supporting Information is available from the Wiley Online Library or from the author.

## Acknowledgements

D.F. and X.S. contributed equally to this work. The authors acknowledge the funding from the Australian Research Council (CE230100032, S.-Z.Q.,

Y.Z.; DP230102027, S.-Z.Q.; DP240102575, Y.Z.). D.F. acknowledges the financial support from the Chinese CSC scholarship Program. The authors acknowledge support from the X-ray Absorption Spectroscopy beamline at the Australian Synchrotron, ANSTO, Melbourne.

## Conflict of Interest

The authors declare no conflict of interest.

## Data Availability Statement

The data that support the findings of this study are available from the corresponding author upon reasonable request.

## Keywords

alkaline seawater electrolysis, molybdate anchoring, oxygen vacancies, startup-shutdown stability

Received: October 2, 2025

Revised: November 30, 2025

Published online:

- [1] N. K. Shrestha, S. A. Patil, J. Han, S. Cho, A. I. Inamdar, H. Kim, H. Im, *J. Mater. Chem. A* **2022**, *10*, 8989.
- [2] S. A. Patil, D. V. Patil, P. Katkar, S. Hussain, G. Nazir, S. Cho, A. I. Inamdar, H. Im, N. K. Shrestha, *Energy Fuels* **2024**, *38*, 22393.
- [3] W. Tong, M. Forster, F. Dionigi, S. Dresp, R. Sadeghi Erami, P. Strasser, A. J. Cowan, P. Farràs, *Nat. Energy* **2020**, *5*, 367.
- [4] S. A. Patil, A. C. Khot, V. D. Chavan, I. Rabani, D. K. Kim, J. Jung, H. Im, N. K. Shrestha, *Chem. Eng. J.* **2024**, *480*, 146545.
- [5] W. Xu, Z. Wang, P. Liu, X. Tang, S. Zhang, H. Chen, Q. Yang, X. Chen, Z. Tian, S. Dai, L. Chen, Z. Lu, *Adv. Mater.* **2024**, *36*, 2306062.
- [6] F. Yang, Y. Luo, Q. Yu, Z. Zhang, S. Zhang, Z. Liu, W. Ren, H. M. Cheng, J. Li, B. Liu, *Funct. Mater.* **2021**, *31*, 2010367.
- [7] Y. Chang, L. Kong, D. Xu, X. Lu, S. Wang, Y. Li, J. Bao, Y. Wang, Y. Liu, *Chemie Int.* **2024**, *33*, 2211174.
- [8] X. Kang, F. Yang, Z. Zhang, H. Liu, S. Ge, S. Hu, S. Li, Y. Luo, Q. Yu, Z. Liu, Q. Wang, W. Ren, C. Sun, H. M. Cheng, B. Liu, *Nat. Commun.* **2023**, *14*, 3607.
- [9] X. Yang, H. Shen, X. Xiao, Z. Li, H. Liang, S. Chen, Y. Sun, B. Jiang, G. Wen, S. Wang, L. Zhang, *Adv. Mater.* **2025**, *37*, 2416658.
- [10] L. Shao, X. Han, L. Shi, T. Wang, Y. Zhang, Z. Jiang, Z. Yin, X. Zheng, J. Li, X. Han, Y. Deng, *Adv. Energy Mater.* **2024**, *14*, 2303261.
- [11] Q. Sha, S. Wang, L. Yan, Y. Feng, Z. Zhang, S. Li, X. Guo, T. Li, H. Li, Z. Zhuang, D. Zhou, B. Liu, X. Sun, *Nature* **2025**, *639*, 360.
- [12] G. Qian, J. Chen, T. Yu, J. Liu, L. Luo, S. Yin, *Nano-Micro Lett.* **2022**, *14*, 20.
- [13] C. Huang, L. Yu, W. Zhang, Q. Xiao, J. Zhou, Y. Zhang, P. An, J. Zhang, Y. Yu, *Appl. Catal. B Environ.* **2020**, *276*, 119137.
- [14] W. Du, Y. Shi, W. Zhou, Y. Yu, B. Zhang, *Angew. Chem., Int. Ed.* **2021**, *60*, 7051.
- [15] Q. Liu, W. Bi, J. Guan, C. Xiao, Y. Xie, *Mater. Chem. Front.* **2023**, *7*, 5957.
- [16] I. S. Kim, H. S. Cho, M. Kim, H. J. Oh, S. Y. Lee, Y. K. Lee, C. Lee, J. H. Lee, W. C. Cho, S. K. Kim, J. H. Joo, C. H. Kim, *J. Mater. Chem. A* **2021**, *9*, 16713.
- [17] M. Mehdi, B. S. An, H. Kim, S. Lee, C. Lee, M. Seo, M. W. Noh, W. C. Cho, C. H. Kim, C. H. Choi, B. H. Kim, M. J. Kim, H. S. Cho, *Adv. Energy Mater.* **2023**, *13*, 2204403.

- [18] Y. Kim, S. M. Jung, K. S. Kim, H. Y. Kim, J. Kwon, J. Lee, H. S. Cho, Y. T. Kim, *JACS Au* **2022**, *2*, 2491.
- [19] S. M. Jung, Y. Kim, B. J. Lee, H. Jung, J. Kwon, J. Lee, K. S. Kim, Y. W. Kim, K. J. Kim, H. S. Cho, J. H. Park, J. W. Han, Y. T. Kim, *Adv. Funct. Mater.* **2024**, *34*, 2316150.
- [20] X. Sun, W. Shen, H. Liu, P. Xi, M. Jaroniec, Y. Zheng, S. Z. Qiao, *Nat. Commun.* **2024**, *15*, 10351.
- [21] S. Zhang, Y. Wang, S. Li, Z. Wang, H. Chen, L. Yi, X. Chen, Q. Yang, W. Xu, A. Wang, Z. Lu, *Nat. Commun.* **2023**, *14*, 4822.
- [22] D. Liu, X. Wei, J. Lu, X. Wang, K. Liu, Y. Cai, Y. Qi, L. Wang, H. Ai, Z. Wang, *Mater.* **2024**, *36*, 2408982.
- [23] A. Rajput, A. Kumari, H. K. Basak, D. Ghosh, B. Chakraborty, *J. Mater. Chem. A* **2024**, *12*, 30810.
- [24] Z. Li, Y. Zheng, W. Zu, L. Dong, L. Y. S. Lee, *Adv. Sci.* **2025**, *12*, 2410911.
- [25] W. Guo, C. Dun, M. A. Marcus, V. Venturi, Z. Gainsforth, F. Yang, X. Feng, V. Viswanathan, J. J. Urban, C. Yu, Q. Zhang, J. Guo, J. Qiu, *Adv. Mater.* **2023**, *35*, 2211603.
- [26] J. Zhang, Y. Ye, Z. Wang, Y. Xu, L. Gui, B. He, L. Zhao, *Adv. Sci.* **2022**, *9*, 2201916.
- [27] Y. Chen, Y. Wang, B. Liu, C. Zhang, D. Sun, H. Liu, W. Zhou, *J. Colloid Interface Sci.* **2024**, *664*, 469.
- [28] N. K. Shrestha, A. I. Inamdar, H. Im, S. Cho, *J. Mater. Chem. A* **2024**, *12*, 29978.
- [29] X. Xie, C. Y. Chan, W. A. Daoud, *J. Mater. Chem. A* **2021**, *9*, 24943.
- [30] Z. Wang, J. Chen, E. Song, N. Wang, J. Dong, X. Zhang, P. M. Ajayan, W. Yao, C. Wang, J. Liu, J. Shen, M. Ye, *Nat. Commun.* **2021**, *12*, 5960.
- [31] H. Li, Z. Li, Z. Li, Z. Zhang, C. Li, J. Wang, *J. Mater. Chem. A* **2023**, *11*, 20102.
- [32] Y. Yang, W. Zheng, P. Wang, Z. Cheng, P. Wang, J. Yang, C. Wang, J. Chen, Y. Qu, D. Wang, Q. Chen, *ACS Nano* **2024**, *18*, 24458.
- [33] K. Auewattanapun, J. P. S. Bermundo, U. Hanifah, H. Nakajima, W. Limphirat, R. Techapiesancharoenkij, Y. Uraoka, *ACS Appl. Mater. Interfaces* **2024**, *16*, 60521.
- [34] C. Triolo, K. Moulaee, A. Ponti, G. Pagot, V. Di Noto, N. Pinna, G. Neri, S. Santangelo, *Adv. Funct. Mater.* **2024**, *34*, 2306375.
- [35] R. A. Senthil, S. Jung, A. Min, A. Kumar, C. J. Moon, M. Singh, M. Y. Choi, *ACS Catal.* **2024**, *14*, 3320.
- [36] Q. Qin, H. Jiang, X. Jiang, L. Wang, X. Wang, M. G. Kim, S. Liu, X. Liu, J. Cho, *Chemie Int. Ed.* **2024**, *63*, 202317622.
- [37] C. Lang, Y. Xu, X. Yao, *Chinese J. Catal.* **2024**, *64*, 4.
- [38] G. Lin, A. Dong, Z. Li, W. Li, X. Cao, Y. Zhao, L. Wang, L. Sun, *Adv. Mater.* **2025**, *37*, 2507525.
- [39] Z. Zhu, L. Luo, Y. He, M. Mushtaq, J. Li, H. Yang, Z. Khanam, J. Qu, Z. Wang, M. S. Balogun, *Adv. Funct. Mater.* **2024**, *34*, 2306061.
- [40] Z. Zhao, J. Sun, Z. Li, X. Xu, Z. Zhang, C. Li, L. Wang, X. Meng, *J. Mater. Chem. A* **2023**, *11*, 10346.
- [41] Y. Zhao, J. Li, K. Li, L. Liang, J. Zhu, M. Xiao, C. Liu, W. Xing, *Mater. Chem. A* **2025**, *13*, 9184.
- [42] L. Yu, Q. Zhu, S. Song, B. McElhenney, D. Wang, C. Wu, Z. Qin, J. Bao, Y. Yu, S. Chen, Z. Ren, *Nat. Commun.* **2019**, *10*, 5106.
- [43] W. Xu, T. Ma, H. Chen, D. Pan, Z. Wang, S. Zhang, P. Zhang, S. Bao, Q. Yang, L. Zhou, Z. Tian, S. Dai, Z. Lu, *Adv. Funct. Mater.* **2023**, *33*, 2302263.
- [44] J. Sun, G. Ren, S. Qin, Z. Zhao, Z. Li, Z. Zhang, C. Li, X. Meng, *Nano Energy* **2024**, *121*, 109246.
- [45] J. Liu, X. Liu, H. Shi, J. Luo, L. Wang, J. Liang, S. Li, L. M. Yang, T. Wang, Y. Huang, Q. Li, *Appl. Catal. B Environ.* **2022**, *302*, 120862.
- [46] M. Li, H. Li, H. Fan, Q. Liu, Z. Yan, A. Wang, B. Yang, E. Wang, *Nat. Commun.* **2024**, *15*, 6154.
- [47] W. Hao, X. Ma, L. Wang, Y. Guo, Q. Bi, J. Fan, H. Li, G. Li, *Adv. Energy Mater.* **2024**, *15*, 2403009.
- [48] J. Fan, X. Ma, J. Xia, L. Zhang, Q. Bi, W. Hao, *J. Colloid Interface Sci.* **2024**, *657*, 393.
- [49] W. Xie, J. Huang, L. Huang, S. Geng, S. Song, P. Tsikararas, Y. Wang, *Appl. Catal. B Environ.* **2022**, *303*, 120871.
- [50] Z. Cen, F. Yang, J. Wan, K. Xu, *Chem. Commun.* **2023**, *59*, 8708.
- [51] K. Ham, S. Hong, S. Kang, K. Cho, J. Lee, *ACS Energy Lett.* **2021**, *6*, 364.
- [52] J. Kim, S. M. Jung, H. Im, H. Hwang, D. S. Kim, G. W. Jeon, Y. T. Kim, J. W. Han, J. K. Kim, *Chem. Eng. J.* **2024**, *501*, 157385.
- [53] H. yu Guo, X. qi Gao, K. chang Yu, X. mao Wang, S. ming Liu, *Sep. Purif. Technol.* **2023**, *326*, 124830.
- [54] Z. Xu, J. Wang, J. Qiu, H. Cao, Y. Xie, *Environ. Sci. Technol.* **2023**, *57*, 14442.
- [55] Q. Zhang, W. Xiao, J. X. Shi, J. L. Lei, Q. Xiao, H. Q. Luo, N. B. Li, *ACS Catal.* **2024**, *14*, 18003.
- [56] B. Lu, Z. Li, J. Yin, K. Zhu, K. Ye, *Catal. B Environ.* **2024**, *350*, 123940.
- [57] Z. Liang, D. Shen, Y. Wei, F. Sun, Y. Xie, L. Wang, H. Fu, *Adv. Mater.* **2024**, *36*, 2408634.
- [58] K. Panigrahi, S. Mal, S. Bhattacharyya, *J. Mater. Chem. A* **2024**, *12*, 14334.
- [59] R. J. Gomes, R. Kumar, H. Fejzić, B. Sarkar, I. Roy, C. V. Amanchukwu, *Nat. Catal.* **2024**, *7*, 689.
- [60] J. Mu, C. Yu, X. Song, L. Chen, J. Zhao, J. Qiu, *Adv. Funct. Mater.* **2025**, *35*, 2423965.